Laplacian and caustic imaging theories of MEM work-function contrast

S. M. Kennedy
D. E. Jesson
D. M. Paganin

We apply geometrical, Laplacian, and caustic imaging theories to simulate the mirror electron microscope (MEM) contrast arising from a surface phase boundary associated with a discontinuity in work function. The key approximations inherent in the theories are highlighted and investigated within strong and weak scattering regimes from the work-function test object. For strongly varying potentials, the approximation that the electron classical turning distance is unchanged fails, invalidating the quantitative accuracy of the geometrical and Laplacian approaches. For sufficiently small defocus and surface height or potential variations, the Laplacian approach facilitates an intuitive interpretation of MEM contrast.

Introduction

Mirror electron microscopy (MEM) is a well-known technique whereby an electron beam is incident on a specimen, which is at a slightly more negative potential than the electron source. Therefore, the beam turns around just above the specimen surface and interacts with the electric field above the specimen. MEM is sensitive to spatial and temporal variations in the electric field close to the surface, which result from the surface topography [1–3] or variations in the electric potential of the specimen, including surface charges, varying conductivity, and contact potentials [4–8]. It has been used to study electric field contrast [6, 7, 9–12], surface magnetic fields [5], and chemical processes at solid surfaces [8, 13]. MEM is a well-established technique that has recently undergone a resurgence, as it is well suited to the recovery of 3-D information and the study of structures that extend hundreds of nanometers from the specimen surface, for example, droplet surface dynamics [14–16].

A number of approaches have been taken to understand and interpret MEM image contrast in order to extract information on the electric field and the underlying surface properties creating it. While some methods apply wave mechanics [17, 18], most treatments have been based on geometrical ray-tracing techniques [4, 6–8, 19–24]. In particular, a geometrical imaging theory has been developed [2, 19, 25, 26] that views MEM contrast as a transverse redistribution of electron current density on an imaging screen. The key assumption of the theory is that the motion of the electron beam along the optical axis, i.e., z, is unchanged by the specimen surface variations. Recently, a Laplacian imaging theory has been developed from the geometrical imaging theory, which applies in the limit of small surface variations and small objective lens defocus Δf [27, 28]. Under these conditions, MEM image contrast is approximately proportional to the transverse Laplacian or curvature of surface height or potential variations blurred slightly to account for the interaction of the electron beam with the field above the surface. Therefore, it provides an intuitive means of interpreting MEM images and may be used to quantitatively recover surface topography where the relevant approximations are applicable [27, 28].

A caustic imaging theory for MEM has been recently developed to treat situations in which the assumptions of the Laplacian imaging theory are not valid [29]. This more general treatment involves tracing a family of electron ray paths through the electric field above the specimen and considering their apparent positions on a virtual imaging plane. Where initially adjacent electron rays cross in the vicinity of the imaging plane, envelopes of ray families known as caustics are created. Caustics lead to very bright features in MEM images, analogous to the bright lines that are formed on the floor of an outdoor swimming pool on a sunny day. As demonstrated in [29], MEM caustics can be used to recover quantitative information on surface topography, for example, the contact angle of a Ga droplet

Digital Object Identifier: 10.1147/JRD.2011.2143310

0018-8646/11/$5.00 © 2011 IBM

on a GaAs surface. While the caustic imaging theory is more broadly applicable than the Laplacian imaging theory, the latter method facilitates a more intuitive interpretation of MEM contrast for small surface variations.

Here, we consider MEM imaging of a test object consisting of a flat surface with two regions of different work functions that meet at a sharp boundary. This might, for example, correspond to a boundary between phases of differing work functions. Image simulations are used to make a quantitative comparison between geometrical, Laplacian, and caustic imaging theories of MEM work-function contrast.

Imaging theories of MEM contrast

Experimental geometry

A schematic of a typical MEM experimental setup is shown in **Figure 1**. An electron beam of energy U passes through anode aperture A of the objective lens. The specimen acts as cathode C of the objective lens and is held at an average voltage of $V < -U/e < 0$, where $-e$ is the electronic charge. Thus, the electron beam turns around above the specimen at a distance

$$\delta = L\left(1 + \frac{U}{eV}\right), \tag{1}$$

where L is the distance between the anode and the cathode. The electric field variations above the specimen surface, due to the variation in the topography or potential of the surface, will deflect the electron trajectories in the vicinity of the turnaround region. The returning electron beam, after exiting anode aperture A, passes through the system, and an image is formed of the electron distribution on the virtual image plane at $z = \Delta f + 4L_M/3$ with objective lens defocus Δf, as shown in Figure 1, with $L_M = L - \delta$. Subscript M denotes "modified."

Geometrical imaging theory

The geometrical imaging theory of MEM contrast [2, 19, 25, 26] describes the image formation as the redistribution of electron positions on the virtual image plane due to the presence of electric field variations above the specimen. Here, we consider a perfectly flat surface with the surface potential varying in one transverse dimension by $\Delta V(x)$ from the potential V of the rest of the surface. In this case, and for parallel illumination of the surface (see Figure 1), the redistribution of electron position is governed by [27, 28]

$$\Delta\tilde{V}_B(x, \delta, \Delta f) = \left(\frac{\Delta f}{8L_M - 3\Delta f}\right)\Delta V(x) \otimes B(x, \delta), \tag{2}$$

where $\Delta\tilde{V}_B(x, \delta, \Delta f)$ is the normalized blurred surface potential variation with units of square meters; $\otimes$ represents convolution in x; and the blurring function B in one dimension is given by [26–28]

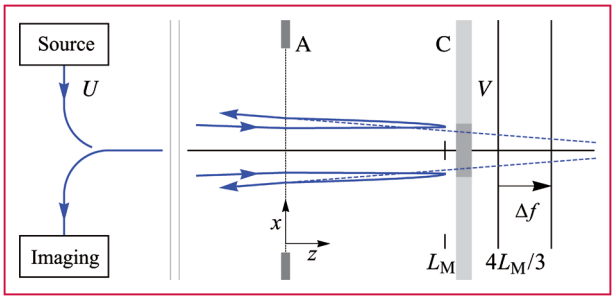

Figure 1

MEM imaging geometry. An electron beam of energy U travels along the z-axis, converging to the point $z = 4L_M$. Anode aperture A acts as a diverging lens, deflecting the electron trajectories as they pass through the aperture to enter and leave the region between A and cathode C. This results in parallel illumination of the sample. The cathode is set at the potential of $V < -U/e < 0$ (lighter shaded region), ensuring that the electron beam turns around in the vicinity of $z = L_M$, a distance of δ before the cathode. The cathode surface may have a variation in work function of ΔV (darker shaded region) compared with the rest of the surface. The turning electron beam is sensitive to deviations in the electric field due to surface and/or potential variations of the specimen. We trace the exiting electron trajectories back along their apparent straight-line paths (dashed lines) to the virtual image plane at $z = \Delta f + 4L_M/3$, which is the object plane for the magnetic objective lens. The left side of the figure, which is separated by double vertical gray lines, is on a much larger scale than the right. Adapted from [28].

$$B(x, \delta) = \frac{-18e\,L_M^{3/2}}{U\sqrt{2}}\sqrt{\frac{\delta + \sqrt{\delta^2 + x^2}}{\sqrt{\delta^2 + x^2}}}. \tag{3}$$

The key assumption of this methodology is that the z motion of the electron (see Figure 1) is unchanged by the electric field variations, so that only transverse variations contribute to the image contrast in MEM [27, 28]. In particular, this assumes that the electron classical turning distance L_M is unchanged, so that the transverse deflection of the electron is obtained via the first derivative of the electric potential above the specimen surface $\phi(x, z)$. For the z-motion assumption to be valid, we therefore require that the difference between $\partial_x\phi(x, z = L_M)$ and $\partial_x\phi(x, z = L'_M)$ be small, where $z = L'_M$ is the maximum departure in turning distance away from L_M, and $\partial_x = \partial/\partial x$. Assuming that this difference is no larger than a fraction ξ of the derivative of the potential, we then have

$$\left|\max_x \partial_x\phi(x, z = L_M) - \max_x \partial_x\phi\left(x, z = L'_M\right)\right| < \xi\left|\max_x \partial_x\phi\left(x, z = L'_M\right)\right|, \tag{4}$$

where $\max_x g(x)$ denotes the maximum value of $g(x)$ over the range of points x.

The intensity of the MEM image for the system shown in Figure 1 is given by [26–28]

$$I(x+\partial_x\Delta\tilde{V}_B,\delta,\Delta f)=I_0(x)/\left|1+\partial_x^2\Delta\tilde{V}_B\right|, \tag{5}$$

where the transverse x derivatives are $\partial_x=\partial/\partial x$ and $\partial_x^2=\partial^2/\partial x^2$, and $I_0(x)$ is the unperturbed intensity distribution on the surface corresponding to $\Delta V=0$ and is typically taken as unity.

Laplacian imaging theory

The Laplacian imaging theory [27, 28] is an approximation to the geometrical theory [see (5)], recovering an intuitive expression for MEM image contrast in terms of the specimen surface height and/or potential variations and the objective lens defocus. To be valid, the Laplacian imaging theory requires that the derivatives of the normalized blurred surface potential variations are small, that is,

$$\left|\partial_x^2\Delta\tilde{V}_B\right|\ll 1, \tag{6}$$

and that the objective lens defocus is sufficiently small to satisfy the inequality

$$|\Delta f|\ll\frac{8L_M}{3+\max_x\left|\partial_x^2(\Delta V(x)\otimes B(x,\delta))\right|}. \tag{7}$$

Provided (6) and (7) are satisfied, we may approximate (5) as [27, 28]

$$\begin{aligned}I(x,\delta,\Delta f)&\approx 1-\partial_x^2\Delta\tilde{V}_B(x,\delta,\Delta f)\\&=1-\frac{\Delta f}{8L_M-3\Delta f}\partial_x^2(\Delta V(x)\otimes B(x,\delta)),\end{aligned} \tag{8}$$

with $I_0(x)=1$. The MEM image contrast under the Laplacian imaging theory is therefore approximately proportional to the objective lens defocus and the second derivative of the surface potential variations, blurred with function B. Note that the Laplacian imaging theory makes the same assumption of unchanged z motion of the electron beam as the geometrical imaging theory [see (4)]. We note that (8) is very similar to the expression for out-of-focus contrast in transmission electron microscopy of thin specimens [30–32].

Equation (8) predicts zero contrast at the defocus $\Delta f=0$, so that nonzero objective lens defocus is required to produce image contrast. To produce a sufficiently large contrast of $\Delta I=I-1$, the minimum required defocus is given by

$$|\Delta f|>\frac{8L_M\Delta I}{3\Delta I+\max_x\left|\partial_x^2(\Delta V(x)\otimes B(x,\delta))\right|}. \tag{9}$$

Equations (7) and (9) therefore give the upper and lower limits of the suitable defocus range for the Laplacian imaging theory, respectively.

Caustic imaging theory

Unlike the geometrical and Laplacian imaging theories, the caustic imaging theory [29] does not assume that the z motion of the electron beam is unaffected by the electric field variations above the specimen surface. Instead, the electric potential above the specimen surface $\phi(x,z)$ is found by solving Laplace's equation in two dimensions, i.e.,

$$\frac{\partial^2\phi}{\partial x^2}+\frac{\partial^2\phi}{\partial z^2}=0, \tag{10}$$

which may be analytically soluble for specific cases of ΔV but, in general, must be numerically solved, for example, using finite-element methods [29, 33]. A family of electron ray trajectories is then traced through the resulting electric field $\mathbf{E}=(-\partial\phi/\partial x,-\partial\phi/\partial z)$ using a fourth-order Runge–Kutta method [24, 29, 34]. The incident electron paths start at $z=0$ with an equal spacing between rays of x_0 along the transverse x-axis (the vertical axis of Figure 1). The rays, initially traveling parallel to the z-axis, are traced through the turning region and back to the anode aperture. We then project back along the apparent straight-line paths of the emerging rays to the virtual image plane at $z=\Delta f+4L_M/3$, as shown Figure 1. We simulate the MEM image intensity at this image plane by comparing the distance between two adjacent rays, i.e., $s(x,\delta,\Delta f)$, with the equal spacing expected for an equipotential flat specimen $\Delta V=0$ [29], i.e.,

$$I(x,\delta,\Delta f)=\frac{x_0\left(\frac{2}{3}-\frac{\Delta f}{4L_M}\right)}{s(x,\delta,\Delta f)}. \tag{11}$$

Where initially adjacent rays cross ($s\to 0$), the intensity is theoretically infinite but, in practice, results in a region of very high intensity, creating a very bright region or caustic in the image [29–33]. Examples of caustics in experimental MEM images include [14, Figure 1], [15, Figures 1 and 3], [16, Figure 2], [24, Figure 1], and [29, Figure 3].

Electric potential due to work-function variation

As a test object, we consider a spatial variation in work function that might, for example, correspond to separate surface phases. We take the surface potential of a flat specimen as

$$\phi(x,z=L)=V+\Delta V(x), \tag{12}$$

where the surface potential variation is

$$\Delta V(x)=\begin{cases}V_0, & P\le x\le Q\\ 0, & x<P,\ x>Q\end{cases} \tag{13}$$

for points P and Q on the x-axis that act as the boundaries between regions with differing work functions, here taken as $P=-8.5$ μm and $Q=1.5$ μm. Thus, in the region $P\le x\le Q$, the work function of the specimen differs by

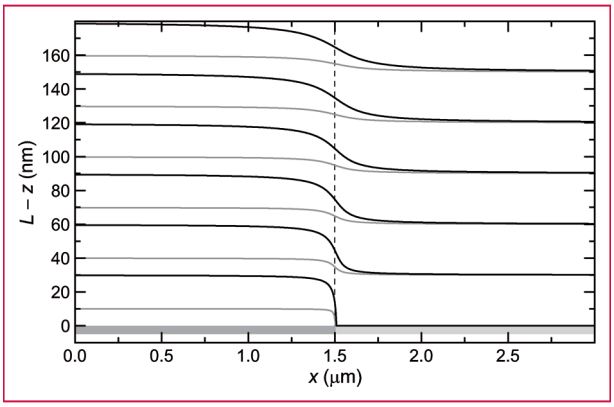

Figure 2

Equipotential surfaces above a flat cathode specimen [see (12)] evaluated using (10) and the finite-element methods package FreeFem++ version 3.9-0 [37]. The potential of the surface ($L - z = 0$ axis) is $V = -20{,}000.4$ V in the lighter gray region and $V = -20{,}000.4 + V_0$ in the darker gray region, where the work-function difference between regions is V_0. The boundary between regions is at $x = 1.5$ μm (dashed line). Equipotential surfaces, beginning at $-20{,}000.4$ V and increasing by 0.3 V intervals, are indicated for (black lines) $V_0 = -0.3$ V and (gray lines) $V_0 = -0.1$ V.

V_0 from the rest of the specimen. We consider the separate cases of $V_0 = -0.3$ V and $V_0 = -0.1$ V, which correspond to typical work-function differences between surfaces phases of GaAs [9, 36].

For this surface, we may solve Laplace's equation analytically via the technique in [27, 28] or numerically via finite-element methods [29]. The results of **Figure 2** were obtained by solving Laplace's equation [see (10)] above the surface in the region -50 μm $\leq x \leq 50$ μm and $0 \leq L - z \leq 120$ μm using the finite-element methods package FreeFem++ version 3.9-0 [37], using mesh adaptation with an interpolation error level of 5×10^{-6}. The potential of the bottom boundary $(L - z = 0)$ is given by (12) with $V_0 = -0.3$ V or $V_0 = -0.1$ V, and the potential of the top boundary is $\phi(x, L - 120\ \mu\text{m}) = -18{,}800.376$ V (as per [29]). The calculated equipotential lines above the specimen surface in the vicinity of the boundary at $x = Q = 1.5$ μm are shown in Figure 2 for the two cases of $V_0 = -0.3$ V and $V_0 = -0.1$ V. The first boundary at P is outside the field of view of Figure 2 and is far enough away that the MEM image contrast of the boundary at Q is not affected.

Caustic image simulations of work-function contrast

To simulate the MEM work-function contrast using the caustic imaging theory, we input 301 rays from $x = -1.125$ μm to $x = 5.625$ μm, which have an equal spacing at $z = 0$ of $x_0 = 0.0225$ μm. These rays are traced

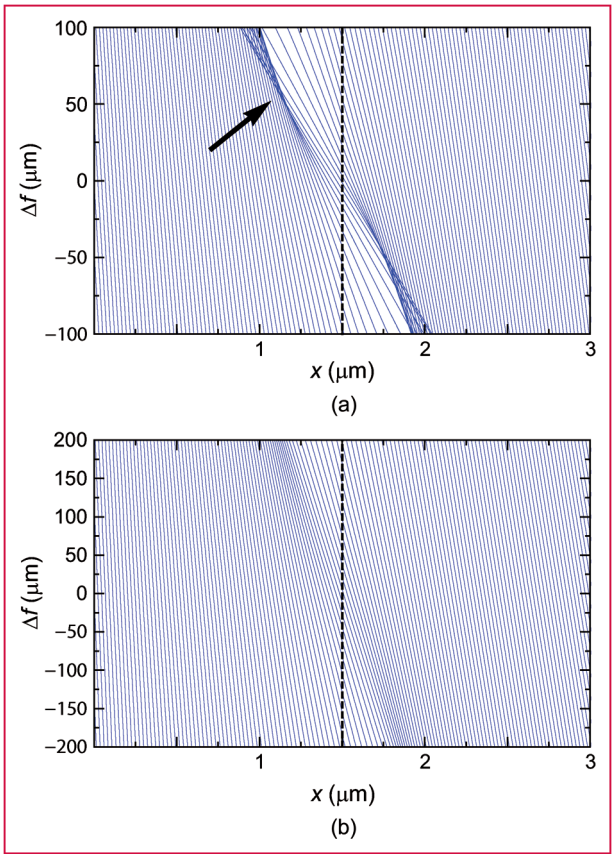

Figure 3

Family of electron ray trajectories on the virtual image plane at $z = \Delta f + 4L_M/3$ (see Figure 1), after interaction with the electric field above a flat surface with a work-function difference [see (12)] of (a) $V_0 = -0.3$ V, $\delta = 40$ nm and (b) $V_0 = -0.1$ V, $\delta = 150$ nm, between two regions with a boundary at $x = 1.5$ μm (dashed line). The crossing of initially adjacent rays creates a fold caustic, and one example is indicated by the arrow in (a). The x positions have been multiplied by 3/2 to account for the demagnification by the anode aperture.

through the electric field of Figure 2 to simulate the MEM image contrast in the vicinity of the boundary at $x = Q = 1.5$ μm. The resulting family of rays on the virtual image plane at $z = \Delta f + 4L_M/3$, which was obtained using a fourth-order Runge–Kutta method [29, 34], is shown in **Figure 3**. To facilitate comparison with the Laplacian imaging theory, we consider two distinct imaging conditions involving "strong" and "weak" scattering from the work-function boundary. The electron beam is assumed to be monochromatic.

Figure 3(a) is an example of strong scattering from the boundary with $V_0 = -0.3$ V. Here, $V = -20{,}000.4$ V, $L = 2$ mm, and $U = 20$ kV, so that the unperturbed $(\Delta V = 0)$ turning distance is $\delta = 40$ nm, and the electron beam will therefore turn around relatively close to the

surface. Where initially adjacent rays cross [e.g., the arrowed region in Figure 3(a)], a caustic is formed, producing very bright image contrast. The caustics in Figure 3(a) are classified as fold caustics [35]. Conversely, we consider weaker scattering from the $V_0 = -0.1$ V boundary in Figure 3(b), with $U = 19,998.9$ V, so that the unperturbed turning distance is $\delta = 150$ nm, and the electron beam turns around further from the surface. Here, the family of rays on the virtual image plane is less dominated by caustic features, and the distribution of rays on either side of the work-function boundary $x = Q = 1.5$ μm is more symmetric.

Comparison of the geometrical, Laplacian, and caustic imaging theories

To compare the geometrical, Laplacian, and caustic imaging theories, we evaluate 1-D MEM image profiles of the work-function boundary defined by (12) and (13) for three values of defocus. Geometrical and Laplacian image simulations are based on (5) and (8), respectively. The caustic image simulations at a specific defocus value correspond to a horizontal section through the ray-trace plots displayed in Figure 3. These are converted into intensity using (11), and we shall assume that this gives an accurate representation of experimental MEM images.

Figure 4(a)–(c) correspond to strong scattering with a work-function difference of $V_0 = -0.3$ V and an unperturbed turning distance of $\delta = 40$ nm above the surface. It can be seen that the caustic imaging theory predicts a bright–dark band pair in the vicinity of the work-function boundary $Q = 1.5$ μm, similar to that of a surface step function [27, 38, 39]. The bright and dark bands reverse position as the defocus changes sign. While the geometrical and Laplacian imaging theories also predict a qualitatively similar bright–dark band pair, both theories overestimate the image contrast and do not match the predicted distance of the bands from the boundary at Q. In addition, the caustic imaging theory predicts strong contrast at zero defocus, whereas the geometrical and Laplacian imaging theories predict zero contrast. However, as defocus changes sign, both theories correctly predict a reversal of the bright and dark band positions.

To explain the differences between theories, we note that, in the geometrical and Laplacian imaging theories, the electron is always assumed to turn around at distance δ from the specimen, despite the stronger electric field in the region $P \le x \le Q$ (see Figure 2) that would force the electron beam as much as 30 nm farther away from the surface. We can quantify this using (4) by evaluating the first derivative of the potential at $z = L_M = L - 40$ nm and at the maximum expected turning point (from Figure 2) $z = L'_M = L - 70$ nm, giving $\xi = 0.44$, which is a significant variation in derivative. The z-motion assumption is therefore invalid, and the geometrical and Laplacian imaging theories allow the electron to penetrate too far into the electric field, overestimating the size of the field in the vicinity of the turnaround region and thus overestimating the image contrast for $V_0 < 0$. Conversely, we note that, in cases where $V_0 > 0$, the geometrical and Laplacian imaging theories will underestimate image contrast. The breakdown of the z-motion assumption is also responsible for the discrepancy between bright and dark band positions in the simulations.

Finally, we note that the differences between the Laplacian and geometrical simulations in Figure 4(a)–(c) for strong scattering can also be explained by a failure to meet Laplacian imaging conditions. In particular, the upper limit of defocus [see (7)] in this case is 17 μm; thus, the condition of (7) cannot be fulfilled while still providing nonzero contrast [e.g., for $|\Delta f| = 10$ μm, as shown in Figure 4(c), we have $|\partial_x^2 \Delta \widetilde{V}_B| = 0.56$ m^{-2}, which does not fulfill (6)]. Therefore, both the Laplacian and geometrical theories are quantitatively inaccurate due to a failure of the z motion approximation, and the two theories also differ with each other due to the inability to meet the Laplacian imaging conditions specified by (6) and (7).

Figure 4(d)–(f) contain the simulated image contrast for $V_0 = 0.1$ V and unperturbed turning distance $\delta = 150$ nm. As shown in Figure 2, the electric field in the vicinity of the electron turning region varies more slowly in x due to both the smaller change in work function and the increased turning distance from the surface. In this weaker scattering regime, there is much closer agreement between the geometrical, Laplacian, and caustic imaging theories in Figure 4(d)–(f) than in Figure 4(a)–(c). This can be explained by the increased validity of the z-motion approximation. Inserting the first derivative of the potential at $z = L_M = L - 150$ nm and $z = L'_M = L - 160$ nm into (4) yields $\xi = 0.19$, which is significantly reduced compared with the previous case of $V_0 = -0.3$ V, $\delta = 40$ nm. In particular, in Figure 4(e), we see that the prediction of zero contrast at zero defocus in the geometrical and Laplacian theories is matched by the caustic imaging theory. Thus, the presence of strong contrast at zero defocus, such as in Figure 4(b), is a clear indication that the z-motion assumption is invalid and that the image contrast may be poorly explained by the geometrical and Laplacian imaging theories.

We note that the conditions for Laplacian imaging given by (6), (7), and (9) are all satisfied, explaining the good agreement between the Laplacian, geometrical, and caustic imaging theories in Figure 4(d)–(f). Quantitatively, these conditions require that the defocus lies within the range of 19 μm and well below 360 μm. Within this regime, surface features may be recovered directly from MEM image contrast (see [27]). We note that even outside the strict domain of validity of the Laplacian imaging theory, it still often remains useful due to the intuitive

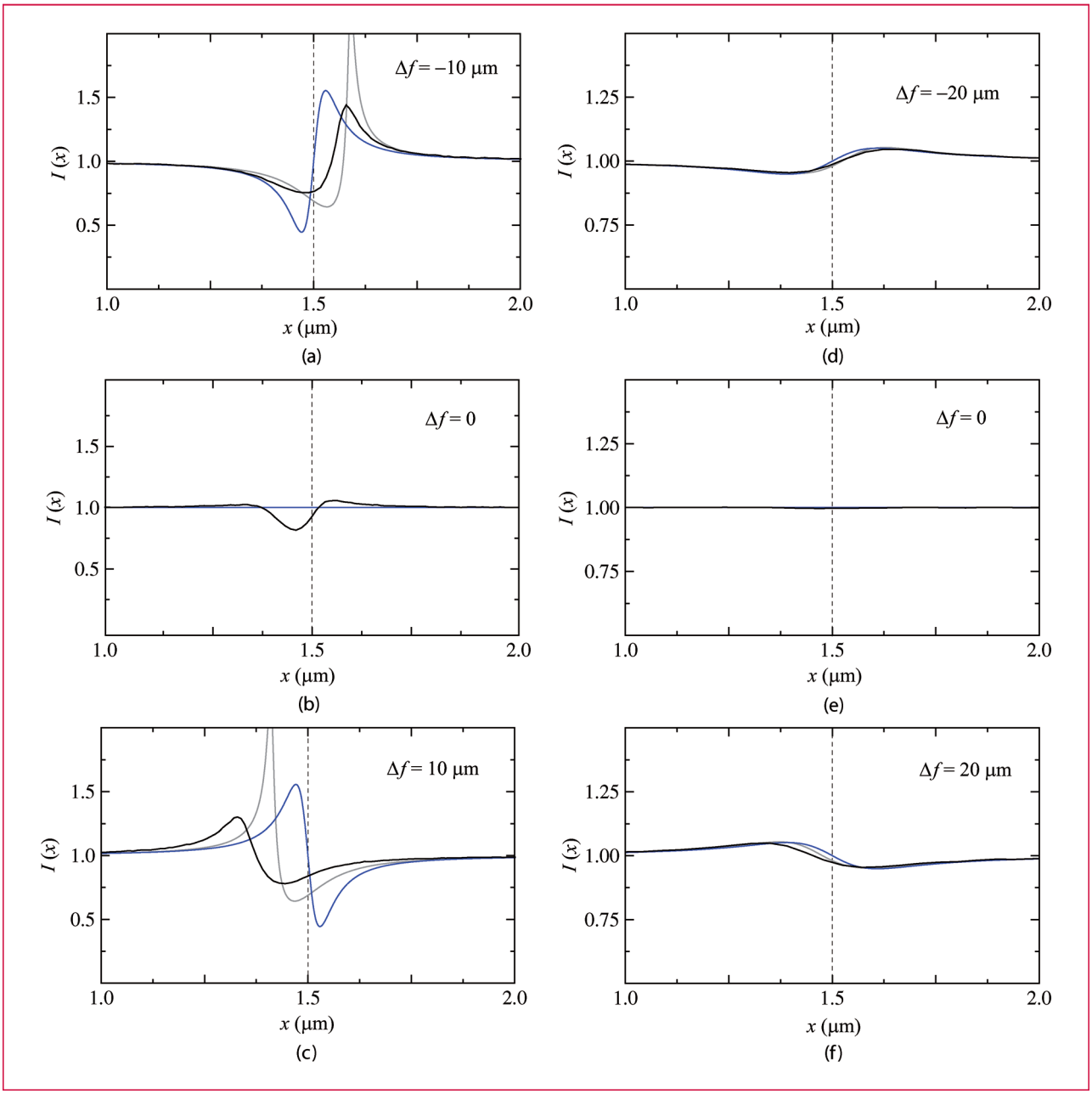

Figure 4

One-dimensional MEM image simulations of a flat surface with a work-function difference of V_0 on either side of a boundary at $x = 1.5$ μm (dashed line). (Blue lines) Laplacian, (black lines) caustic, and (gray lines) geometrical imaging theory simulations are displayed at the indicated defocus values. Panels (a)–(c) correspond to a work-function difference of $V_0 = -0.3$ V and an unperturbed turning distance of $\delta = 40$ nm above the surface, and panels (d)–(f) correspond to $V_0 = -0.1$ V and $\delta = 150$ nm.

connection it draws between surface features and image contrast.

While the electron beam was assumed to be monochromatic, both the Laplacian and caustic imaging theories may be extended to include the effects of a finite energy spread [27–29]. For a Gaussian energy distribution with a full-width at half-maximum of 0.3 eV, the chromatically averaged image contrast was increased by as much as 7% due to the higher energy electrons turning very close to the surface. For the images of Figure 4, this was a small effect and was omitted, but it may be important to include the effects of a finite energy spread at higher resolutions.

Conclusion

We have applied the geometrical, Laplacian, and caustic imaging theories to simulate MEM contrast from a phase boundary associated with a discontinuity in work function. For a large work-function shift and an electron turning point close to the surface, the caustic imaging theory, involving full ray tracing, predicts an asymmetric bright–dark band in the vicinity of the boundary. The geometrical and Laplacian imaging theories lose quantitative accuracy compared with the caustic imaging theory in this strongly scattering regime, as the underlying assumption of unchanged electron motion in the z-direction (perpendicular to the specimen surface) is invalid. With a smaller work-function shift and a turning point further from the surface, the agreement between all theories is much closer. The Laplacian imaging theory is particularly useful in this weak scattering regime because of the intuitive connection it draws between surface features and image contrast, which may also be exploited to directly recover surface features from experimental images.

Acknowledgments

S. M. Kennedy acknowledges funding from the J. L. William Bequest and a Postgraduate Publication Award. D. M. Paganin and D. E. Jesson acknowledge funding from the Australian Research Council via the Discovery Projects program.

References

1. E. Bauer, "LEEM basics," *Surf. Rev. Lett.*, vol. 5, no. 6, pp. 1275–1286, 1998.
2. S. A. Nepijko, N. N. Sedov, and G. Schönhense, "Peculiarities of imaging one- and two-dimensional structures using an electron microscope in the mirror operation mode," *J. Microsc.*, vol. 203, no. 3, pp. 269–276, Sep. 2001.
3. C. C. Speake and C. Trenkel, "Forces between conducting surfaces due to spatial variations of surface potential," *Phys. Rev. Lett.*, vol. 90, no. 16, article no. 160403, Apr. 2003.
4. M. E. Barnett and W. C. Nixon, "Electrical contrast in mirror electron microscopy," *Optik*, vol. 26, pp. 310–325, 1967.
5. M. E. Barnett and W. C. Nixon, "A mirror electron microscope using magnetic lenses," *J. Sci. Instrum.*, vol. 44, no. 11, pp. 893–897, Nov. 1967.
6. A. E. Luk'yanov, G. V. Spivak, and R. S. Gvozdover, "Mirror electron microscopy," *Sov. Phys. Usp.*, vol. 16, no. 4, pp. 529–552, 1974.
7. A. B. Bok, "Mirror electron microscopy theory and applications," in *Diffraction and Imaging Techniques in Material Science*, S. Amelinckx, R. Gevers, and J. Van Landuyt, Eds., 2nd ed. Amsterdam, The Netherlands: North Holland, 1978, pp. 761–788.
8. W. Świêch, B. Rausenberger, W. Engel, A. M. Bradshaw, and E. Zeitler, "In-situ studies of heterogeneous reactions using mirror electron microscopy," *Surf. Sci.*, vol. 294, no. 3, pp. 297–307, Sep. 1993.
9. J. C. Dupuy, A. Sibai, and B. Vilotitch, "Mirror electron microscopy (MEM): Work function and imaging of an electron beam biased junction of silicon (100)," *Surf. Sci.*, vol. 147, no. 1, pp. 191–202, Nov. 1984.
10. J. Slezák, M. Ondejèek, Z. Chvoj, V. Cháb, H. Conrad, S. Heun, T. Schmidt, B. Ressel, and K. C. Prince, "Surface diffusion of Au on Si(111): A microscopic study," *Phys. Rev. B*, vol. 61, no. 23, pp. 16 121–16 128, Jun. 2000.
11. T. Shimakura, Y. Takahashi, M. Sugaya, T. Ohnishi, M. Hasegawa, and H. Ohta, "Mirror electron microscope for inspecting nanometer-sized defects in magnetic media," *Microelectron. Eng.*, vol. 85, no. 8, pp. 1811–1814, Aug. 2008.
12. S. A. Nepijko and G. Schönhense, "Measurement of potential distribution function on object surface by using an electron microscope in the mirror operation mode," *J. Microsc.*, vol. 238, no. 1, pp. 90–94, Apr. 2010.
13. Y. U. Ko and D. C. Joy, "Simulation of imaging in projection microscope using multi-beam probes," *Proc. SPIE*, vol. 4689, pp. 565–575, 2002.
14. E. Hilner, A. A. Zakharov, K. Schulte, P. Kratzer, J. N. Andersen, E. Lundgren, and A. Mikkelsen, "Ordering of the nanoscale step morphology as a mechanism for droplet self-propulsion," *Nano Lett.*, vol. 9, no. 7, pp. 2710–2714, Jul. 2009.
15. J. Tersoff, D. E. Jesson, and W. X. Tang, "Running droplets of gallium from evaporation of gallium arsenide," *Science*, vol. 324, no. 5924, pp. 236–238, Apr. 2009.
16. J. Tersoff, D. E. Jesson, and W. X. Tang, "Decomposition controlled by surface morphology during Langmuir evaporation of GaAs," *Phys. Rev. Lett.*, vol. 105, no. 3, article no. 035702, Jul. 2010.
17. A. J. Hermans and J. A. Petterson, "A quantum mechanical treatment of the mirror electron microscope," *J. Eng. Math.*, vol. 4, no. 2, pp. 141–154, Apr. 1970.
18. S. M. Kennedy, D. E. Jesson, M. J. Morgan, A. E. Smith, and P. F. Barker, "Phase sensitivity of slow electrons to interactions with weak potentials," *Phys. Rev. A*, vol. 74, no. 4, article no. 044701, Oct. 2006.
19. N. N. Sedov, "Théorie quantitative des systèmes en microscopie électronique à balayage, à miroir et à émission," *J. Microsc.-Paris*, vol. 9, pp. 1–26, 1970.
20. T. Someya and J. Kobayashi, "Quantitative application of electron-mirror microscopy to the determination of pure shear of ferroelectric $Gd_2(MoO_4)_3$," *Phys. Stat. Sol. (A)*, vol. 26, no. 1, pp. 325–336, Nov. 1974.
21. G. F. Rempfer and O. H. Griffith, "Emission microscopy and related techniques: Resolution in photoelectron microscopy, low energy electron microscopy and mirror electron microscopy," *Ultramicroscopy*, vol. 47, no. 1–3, pp. 35–54, Nov. 1992.
22. G. F. Rempfer, "Methods of calculating resolution in electron microscopy: Scherzer's equation, circles of least confusion and the intensity distribution approach," *Ultramicroscopy*, vol. 47, no. 1–3, pp. 241–255, Nov. 1992.
23. R. Godehardt, "Mirror electron microscopy," *Adv. Imag. Elect. Phys.*, vol. 94, pp. 81–150, 1995.
24. H.-C. Kan and R. J. Phaneuf, "Focusing of low energy electrons by submicrometer patterned structures in low energy electron microscopy," *J. Vac. Sci. Technol. B*, vol. 19, no. 4, pp. 1158–1163, Jul. 2001.
25. V. G. Dyukov, S. A. Nepijko, and N. N. Sedov, *Electron Microscopy of Local Potentials*. Kiev, Russia: Naukova Dumka, 1991, pp. 10–12, 28–35, 45–51, 63–66, 73–76.
26. S. A. Nepijko and N. N. Sedov, "Aspects of mirror electron microscopy," *Adv. Imag. Electron Phys.*, vol. 102, pp. 273–323, 1997.
27. S. M. Kennedy, C. X. Zheng, W. X. Tang, D. M. Paganin, and D. E. Jesson, "Laplacian image contrast in mirror electron microscopy," *Proc. R. Soc. A.*, vol. 466, no. 2122, pp. 2857–2874, May 2010.
28. S. M. Kennedy, C. X. Zheng, W. X. Tang, D. M. Paganin, and D. E. Jesson, "Laplacian image contrast in mirror electron microscopy (Addendum)," *Proc. R. Soc. A.*, vol. 466, no. 2122, pp. 2857–2874, Oct. 2010.
29. S. M. Kennedy, C. X. Zheng, W. X. Tang, D. M. Paganin, and D. E. Jesson, "Caustic imaging of gallium droplets using mirror electron microscopy," *Ultramicroscopy*, vol. 111, no. 5, pp. 356–363, Apr. 2011.
30. H. Bremmer, "On the asymptotic evaluation of diffraction integrals with a special view to the theory of defocusing and optical contrast," *Physica*, vol. 18, no. 6-7, pp. 469–485, Jun. 1952.

31. J. M. Cowley, *Diffraction Physics,* 3rd ed. Amsterdam, The Netherlands: North Holland, 1995, pp. 26–35, 59–63.
32. J. C. H. Spence, *High-Resolution Electron Microscopy,* 3rd ed. Oxford, U.K.: Oxford Univ. Press, 2003.
33. J. D. Jackson, *Classical Electrodynamics,* 3rd ed. New York: Wiley, 1999, pp. 79–84.
34. W. H. Press, S. A. Teukolsky, W. T. Vetterling, and B. P. Flannery, *Numerical Recipes, the Art of Scientific Computing,* 3rd ed. Cambridge, U.K.: Cambridge Univ. Press, 2007, pp. 229–232, 600–604, 907–910.
35. J. F. Nye, *Natural Focusing and Fine Structure of Light: Caustics and Wave Dislocations*. Bristol, U.K.: Inst. Phys. Publishing, 1999, pp. 9–11, 46–48.
36. J. Massies, P. Etienne, F. Dezaly, and N. T. Linh, "Stoichiometry effects on surface properties of GaAs{100} grown *in situ* by MBE," *Surf. Sci.*, vol. 99, no. 1, pp. 121–131, Sep. 1980.
37. F. Hecht, O. Pironneau, A. Le Hyaric, and J. Morice, *FreeFem++ version 3.9-0*. [Online]. Available: http://www.freefem.org/ff++/
38. M. S. Altman, W. F. Chung, and C. H. Liu, "LEEM phase contrast," *Surf. Rev. Lett.*, vol. 5, no. 6, pp. 1129–1141, 1998.
39. W. F. Chung and M. S. Altman, "Step contrast in low energy electron microscopy," *Ultramicroscopy*, vol. 74, no. 4, pp. 237–246, Sep. 1998.

Received September 30, 2010; accepted for publication February 1, 2011

Shane M. Kennedy *School of Physics, Monash University, Clayton, Victoria 3800, Australia (shane.kennedy@monash.edu).*
Mr. Kennedy received his B.Sc./B.A. degree at Monash University in Australia and submitted his Ph.D. thesis at Monash University at the end of 2010. His thesis focuses on understanding and simulating the processes that produce image contrast in mirror and low-energy electron microscopy.

David E. Jesson *School of Physics, Monash University, Clayton, Victoria 3800, Australia (david.jesson@monash.edu).*
Professor Jesson received his B.Sc. and Ph.D. degrees in physics from Bristol University in the United Kingdom. He has previously held positions at the Council for Scientific and Industrial Research, South Africa; Oak Ridge National Laboratory; and Heriot-Watt University in Edinburgh. He joined Monash University in 2003. His work involves the use of novel electron microscopy techniques to study semiconductor growth mechanisms. Most recently, he has pioneered the development and application of a III-V surface electron microscope.

David M. Paganin *School of Physics, Monash University, Clayton, Victoria 3800, Australia (david.paganin@monash.edu).*
Dr. Paganin received his B.Sc. and Ph.D. degrees in physics from Melbourne University in Australia. He has previously held positions at Melbourne University and CSIRO Australia. He joined Monash in 2002. His work in coherent optics includes a focus on the inverse problem of phase retrieval with a variety of radiation and matter wave fields.